Science Advances

MAAAS

Supplementary Materials for

Twenty-three–millisecond electron spin coherence of erbium ions in a natural-abundance crystal

Marianne Le Dantec, Miloš Rančić, Sen Lin, Eric Billaud, Vishal Ranjan, Daniel Flanigan, Sylvain Bertaina, Thierry Chanelière, Philippe Goldner, Andreas Erb, Ren Bao Liu, Daniel Estève, Denis Vion, Emmanuel Flurin, Patrice Bertet*

*Corresponding author. Email: patrice.bertet@cea.fr

This PDF file includes:

Supplementary Text
Figs. S1 to S12
Tables S1 and S2
References

Supplementary Materials

1 Experimental part

1.1 Standard EPR spectroscopy at $8\,\mathrm{K}$

The identification of the impurities present in $CaWO_4$ is achieved using a conventional EPR spectrometer (Bruker EMX) operating at $9.63\,\mathrm{GHz}$. The angular dependence is measured using an automatic goniometer with a relative resolution $< 1°$. The sample is mounted such that $60°$ ($150°$) corresponds to $\mathbf{B_0}$//a ($\mathbf{B_0}$//c). A temperature of $8\,\mathrm{K}$ is chosen in order to optimise the signal-to-noise ratio for a range of paramagnetic impurities with varying spin relaxation rates.

Four Kramers rare-earth-ions (Er^{3+}, Ce^{3+}, Yb^{3+}, Nd^{3+}) are identified based on known anisotropic g-tensors (*27*), which are simulated with open-circles in Fig. S1. The isotropic line at $B_0 = 160\,\mathrm{mT}$ is attributed to Fe^{3+} ions (*41*). The relative concentration of these species with respect to erbium is estimated within an error of 10%: [Yb]/[Er]=3.9, [Ce]/[Er]= 54, [Nd]/[Er]=17, [Fe]/[Er]=16. At room temperature Gd^{3+} ions and point defects (vacancies, Schottky type) are also observed. Note that non-Kramers ions such as Eu^{3+}, Ho^{3+}, Tb^{3+} cannot be detected by low field EPR.

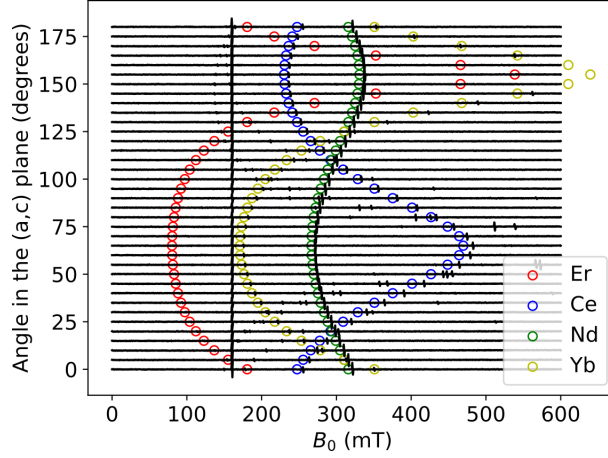Figure S1: **EPR spectroscopy of a sample taken from the same CaWO$_4$ boule recorded at** $\omega_0/2\pi = 9.63\,\text{GHz}$ **and 8 K.** We identify four rare-earth ions (open circles): erbium, cerium, neodymium and ytterbium, whose g-factors in CaWO$_4$ are taken from (*27*). The strong signal at $160\,\text{mT}$ could be iron ions (*41*).

1.2 Resonator design

Three superconducting micro-resonators are fabricated with similar designs, in order to target slightly different frequencies. Each resonator consists in two lumped elements: an interdigitated capacitor C shunted by a central inductance wire L. Table S1 shows the resonator geometric properties: wire width w, wire length l, finger width W and number of pairs of interdigitated fingers N.

resonator design	reso 1	reso 2	reso 3
w (μm)	2	5	5
l (μm)	630	720	630
W (μm)	10	50	10
N	8	6	8

Table S1: **Resonator geometric properties.**

Table S2 also indicates the frequency ω_0, the coupling quality factor Q_c, the internal quality factor Q_i at single photon intra-resonator field, and total quality factor $Q_t = (1/Q_c + 1/Q_i)^{-1}$,
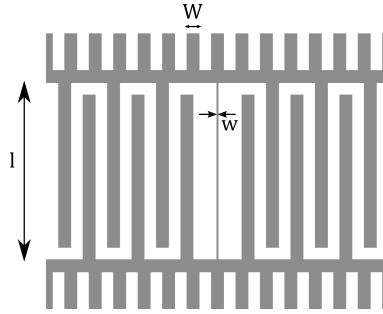
Figure S2: **Example resonator design (resonator 2) with key tunable design parameters W, w and l labeled.**

all measured at $10\,\mathrm{mK}$ and zero magnetic field. These parameters were found to slightly vary from one experimental run to another.

resonator property	reso 1	reso 2	reso 3
$\omega_0/2\pi$ (GHz)	7.025	7.508	7.881
Q_c (/1000)	250	15	29
Q_i (/1000)	45	70	100
Q_t (/1000)	38	12	22

Table S2: **Resonator properties measured at 10 mK and zero magnetic field.**

The resonator frequency decreases by approximately $1\,\mathrm{MHz}$ at $70\,\mathrm{mT}$, due to kinetic inductance and an out-of-plane magnetic field component which could not be compensated for.

1.3 EPR spectroscopy at $10\,\mathrm{mK}$ and rotation pattern in the crystallographic ab plane

Microwave absorption is detected using Hahn-echo sequences ($\pi/2-\tau-\pi-\tau-$echo) for a fixed magnetic field $\mathbf{B_0}$, which is generated by two perpendicular home-made Helmholtz coils. Short delays of $\tau \sim 30\text{-}40\,\mu\mathrm{s}$ are used between pulses to prevent loss of signal due to decoherence effects (refer to section 1.6 for more details). Spectra are then developed by stepping $\mathbf{B_0}$ and repeating the Hahn-echo measurement at each step.
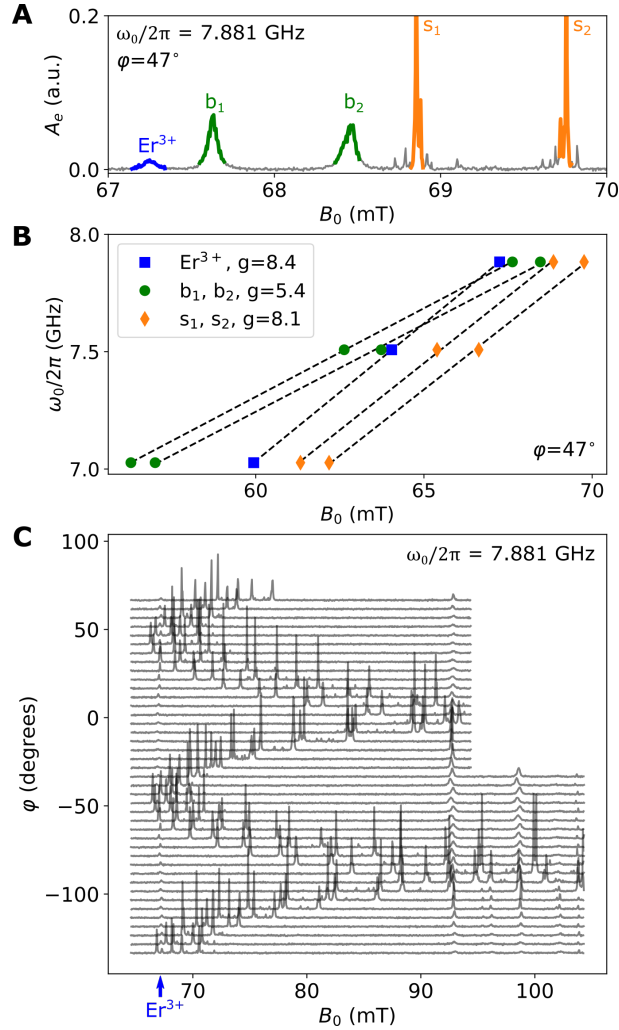
Figure S3: **Hahn-echo spectroscopy at 10 mK.** (A) Spectrum recorded with the resonator at highest frequency $\omega_0/2\pi = 7.881$ GHz and with magnetic field angle $\varphi = 47°$. The erbium line is the peak at 67.2 mT. Pairs of broad peaks (b_1, b_2) and of sharp peaks (s_1, s_2) are also observed. This spectroscopy is repeated for the three resonators in order to measure the field-frequency curves in (B). (B) Resonance frequency as a function of the magnetic field B_0 for each of the five transitions detected in (A), where $\varphi = 47°$. Dashed black lines are linear fits which give the g-factor shown in the legend within a standard error of 3%. (C) Rotation pattern in the ab plane with the resonator at highest frequency $\omega_0/2\pi = 7.881$ GHz. The erbium line is the smaller peak at 67.2 mT and its resonance frequency is independent of φ as expected. The pairs (b_1, b_2) and (s_1, s_2) demonstrate a strong angular dependence in the ab plane.

For the resonator at frequency $\omega_0/2\pi = 7.881\,\text{GHz}$, the erbium transition is expected at $B_0 = 67.2\,\text{mT}$. When the magnetic field is approximately aligned with the resonator inductance wire ($\varphi \sim 50°$), we detect other electron spin transitions in the vicinity of the erbium transition, in particular a pair of broad peaks (b_1, b_2) and sharp peaks (s_1, s_2), as shown in Fig. S3A. In order to confirm that the smallest peak at $67.2\,\text{mT}$ corresponds to erbium, the spectroscopy of Fig. S3A is repeated for all three resonators. In this way, it is possible to extract the effective g-factor of each transition from the value of their frequency as a function of B_0. As shown in Fig. S3B, only one peak is consistent (within error) with the g-factor of erbium g$_\perp$=8.38.

Moreover a field rotation in the ab plane is performed with the resonator at frequency $\omega_0/2\pi = 7.881\,\text{GHz}$ in Fig. S3C and shows a strong variation of the gyromagnetic ratios of the pairs of peaks (b_1, b_2, s_1, s_2). These peaks indicate dopants in a non-tetragonal site. The slight asymmetry of the rotation pattern with respect to $\varphi = 0°$ might be caused by a weak magnetic field component along the crystal c-axis. Isotropic lines between 90 and $100\,\text{mT}$ are also identified, albeit without sufficient spectroscopic information to determine the impurity in question.

Lastly, a transition at $B_0 = 37.05\,\text{mT}$ is also observed with the resonator at $\omega_0/2\pi = 7.508\,\text{GHz}$. This is consistent (within error) with the first hyperfine level of ^{167}Er. The spin-echo spectroscopy at $10\,\text{mK}$ is shown in Fig. S4.
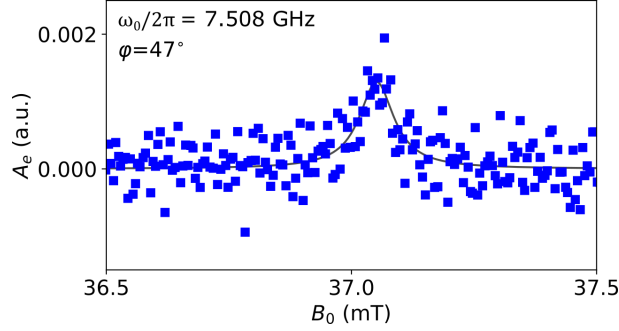
Figure S4: **Hahn-echo spectroscopy over the first hyperfine transition of ^{167}Er.** The Lorentzian fit (solid line) gives a full-width-at-half-maximum of $0.09 \pm 0.01\,\text{mT}$ which corresponds to a linewidth of $\Gamma/2\pi = 10 \pm 1\,\text{MHz}$.

1.4 Angular dependence of absorption linewidth

As explained by Mims and Gillen (*26, 27*), when the magnetic field $\mathbf{B_0}$ is applied in the ab plane, only the c-axis component E_c of an electric field will lift the degeneracy of the g-factor $\text{g}_\perp$ in the ab plane, such that

$$\delta\text{g}_\perp^2 = 2\text{g}_\perp \delta\text{g}_\perp = \alpha \sin\left(2\varphi - 2\varphi_0\right)E_c, \tag{1}$$

where $\alpha = (11 \pm 0.6) \times 10^{-6}\,(\text{V/cm})^{-1}$ and $\varphi_0 = 31 \pm 1°$ for Er^{3+}:CaWO$_4$.

The shift in resonance frequency is then

$$\delta\omega = \delta\text{g}_\perp \frac{\mu_B}{\hbar} B_0, \tag{2}$$

where μ_B is the Bohr magneton and the sensitivity of the spin-transition frequency to electric fields is

$$\frac{\partial\omega}{\partial E_c} = \frac{\alpha \sin\left(2\varphi - 2\varphi_0\right)}{2\text{g}_\perp} \frac{\mu_B}{\hbar} B_0. \tag{3}$$

Now, if each of the erbium ion sees a random electric field of the order of ΔE_c along the c-axis, possibly due to charge defects in the CaWO$_4$ crystal as assumed in (*26*), the full-width-at-half-maximum of the transition linewidth of the spin-ensemble broadens such that

$$\Gamma \sim \Gamma_{\text{min}} + |\frac{\partial\omega}{\partial E_c}|\Delta E_c. \tag{4}$$

Fitting this formula to the data of Fig. 1E leads to $\Delta E_c = 32.0 \pm 0.6$ kV/cm. This value is approximately three times smaller than measured by Mims and Gillen in their ppm doped crystal (26), a difference that could be attributed to our lower doping concentration, and hence reduced charge defect density. Moreover, the fit also confirms that the spin transition frequency becomes insensitive to E_c at $\varphi = \varphi_0 = 31°$.

1.5 Estimation of the erbium concentration

Determining the density of Er^{3+} ions in the crystal is achieved by measuring the coupling between the erbium spin-ensemble and the microwave resonator. To do so, a complex microwave reflection measurement $r(\omega)$ was recorded on a Vector Network Analyser (VNA). As explained in ref. (42), when the microwave resonator is coupled to a spin ensemble of Lorentzian lineshape with coupling g_{ens}, the reflection coefficient can be expressed as

$$r(\omega) = \frac{i\kappa_c}{(\omega - \omega_0) + i\frac{\kappa_c + \kappa_{\text{int}}}{2} - \frac{g_{\text{ens}}^2}{(\omega - \omega_s) + i\frac{\Gamma}{2}}} - 1, \tag{5}$$

where ω_0, κ_c and κ_{int} are the frequency, coupling rate and loss rate of the resonator and ω_s and Γ are the spin transition frequency and inhomogeneous linewidth, respectively.

In particular, the spin ensemble broadens the resonance linewidth according to

$$\tilde{\kappa}_{\text{int}} = \kappa_{\text{int}} + \frac{g_{\text{ens}}^2 \Gamma}{(\omega - \omega_s)^2 + (\Gamma/2)^2}. \tag{6}$$

The measured internal quality factor is shown in Fig. S5 and the fit with $Q_i = \omega_0/\tilde{\kappa}_{\text{int}}$ (43) yields an ensemble coupling at low input power of $g_{\text{ens}}/2\pi = 140 \pm 6$ kHz.

The concentration ρ of the zero nuclear-spin isotopes of erbium is then estimated by considering how g_{ens} depends on the spatial variation of vacuum magnetic field fluctuations under the resonator (44)

$$g_{\text{ens}} = \frac{\mu_B}{2\hbar} \sqrt{\rho \int_V \mathbf{dr} (g_\parallel \delta B_{1z}(\mathbf{r}))^2 + (g_\perp \cos(\Delta\varphi) \delta B_{1y}(\mathbf{r}))^2} \tag{7}$$
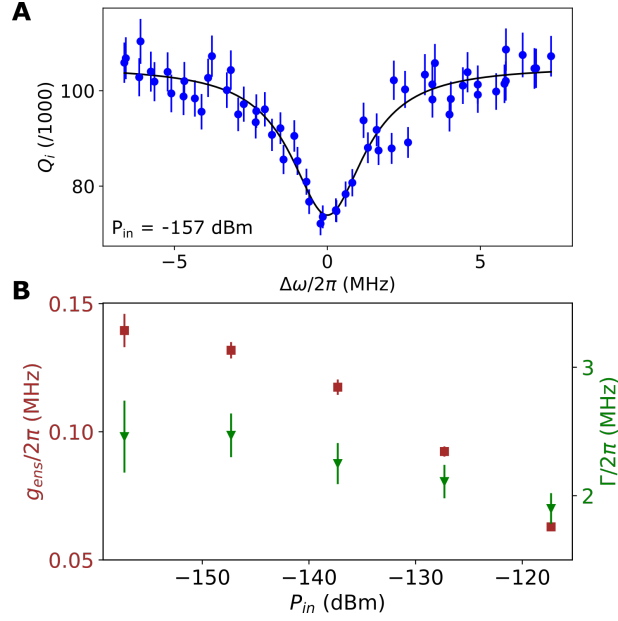
Figure S5: **Continuous-wave spectroscopy at 10 mK.** (**A**) Internal quality factor Q_i as a function of B_0, around $67.2 \, \text{mT}$, and converted into a frequency detuning $\Delta\omega$, measured with input power P_{in} at the sample of $-157 \, \text{dBm}$. φ is set to $30°$. Solid black line is a fit to the data. (**B**) Fitted ensemble coupling g_{ens} and linewidth Γ as functions of P_{in}. As the input power decreases, the ensemble coupling g_{ens} saturates at $g_{\text{ens}}/2\pi = 140 \pm 6 \, \text{kHz}$.

where $\Delta\varphi = \varphi - \varphi_{\text{w}} = 21°$ is the angle between $\mathbf{B_0}$ and the resonator wire axis.

From this equation, we estimate $\rho = (0.7 \pm 0.1) \times 10^{13} \, \text{cm}^{-3}$. This corresponds to a total trivalent erbium concentration (including all isotopes) of $[\text{Er}^{3+}] = \frac{\rho}{0.77} = 0.7 \pm 0.1 \, \text{ppb}$.

1.6 Homogeneous phase noise and $\mathbf{T_2}$ measurements

We measure spin echoes using homodyne detection and obtain two field quadratures whose constant offsets are subtracted, yielding $I(t)$ and $Q(t)$. The echo has a phase θ in the IQ plane which depends ideally only on the phase of the driving pulses. In order to have the best signal-to-noise ratio, the echo amplitude is often computed using an average of N individual echo traces as follows

$$A_{e,\text{phase}} = \text{Re} \, (e^{-i\theta} \frac{1}{N} \sum_{n=1}^{N} \{ \int_t [I_n(t) + iQ_n(t)] dt \}). \tag{8}$$

However, when using a Hahn-echo sequence ($\pi/2 - \tau - \pi - \tau-$echo), we observe in our measurements that the echo phase θ varies from trace to trace when the delay τ becomes larger than about $1\,\mathrm{ms}$. As observed in other related experiments (*33*), we attribute this to noise in the applied magnetic field $\mathbf{B_0}$ in the 100 Hz-10 kHz frequency band that modulates the ensemble transition frequency, thus randomizing θ for $\tau > 2\,\mathrm{ms}$.

Therefore, we compute the amplitude of the echo in magnitude, so that it is not sensitive to the echo phase. We choose to compute this magnitude as

$$A_{e,\mathrm{mag}} = \sqrt{\frac{1}{N}\sum_{n=1}^{N}\{[\int_t I_n(t)dt]^2 + [\int_t Q_n(t)dt]^2\}}. \tag{9}$$

Fig. S6 shows the decay of the echo amplitude with the two mentioned averaging methods. When the spin-echo integral A_e is averaged in a phase-sensitive manner, the fitted coherence time $T_{2,\mathrm{phase}}$ is $4.0 \pm 0.2\,\mathrm{ms}$, whereas phase-insensitive averaging yields the correct coherence time $T_{2,\mathrm{mag}} = 23.2 \pm 0.5\,\mathrm{ms}$.
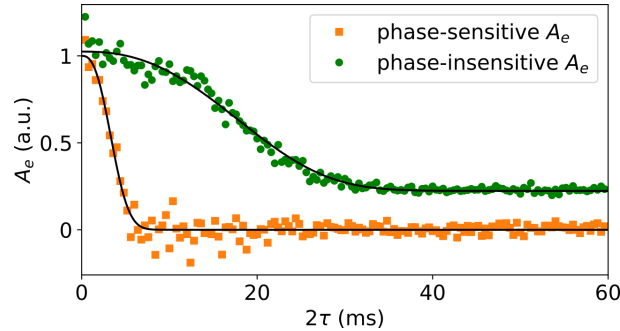

Figure S6: **Electron spin coherence time measurement at 10 mK and $\varphi = 47°$.** The data are averaged either in a phase-sensitive (squares) or insensitive (circles) manner. Solid black lines are fits, the phase-sensitive data being fitted with $A_e = e^{-(2\tau/T_{2,\mathrm{phase}})^{x_{\mathrm{phase}}}}$ and the phase-insensitive data with $A_e = \sqrt{e^{-2(2\tau/T_{2,\mathrm{mag}})^{x_{\mathrm{mag}}}} + C}$. The offset C is a spurious vertical shift corresponding to the variance of the noise and which occurs when averaging the data in magnitude. The fits yield $T_{2,\mathrm{phase}} = 4.0 \pm 0.1\,\mathrm{ms}$, $x_{\mathrm{phase}} = 2.6 \pm 0.2$, $T_{2,\mathrm{mag}} = 23.2 \pm 0.5\,\mathrm{ms}$ and $x_{\mathrm{mag}} = 2.4 \pm 0.1$.

It is well known that spin-coherence can be extended using Dynamical-Decoupling (DD)

techniques such as the Carr-Purcell-Meiboom-Gill (CPMG) sequence (*45*). However, DD sequences requires phase-cycled averaging to suppress spurious stimulated echoes which, in-turn, requires predictable and stable echo signal phase. Therefore, DD measurements were not attempted here due to the observed phase instability in our measurements.

With the exception of coherence time measurements, all data in this article are taken with phase-sensitive averaging, for sufficiently short delays τ yielding negligible fluctuations of the echo phase θ.

1.7 Electron spin-echo envelope modulation (ESEEM)

In Fig. S6, the noise of the data averaged in magnitude seems to decay with the delay 2τ. Complementary measurements record the echo amplitude at short inter-pulse delay τ, with a sampling time of $\Delta\tau = 1\,\mu$s (Fig. S7 and Fig. S8). The time interval for these measurements is $300\,\mu$s and the echo amplitude averaged either in quadrature or magnitude does not decay on this scale as $T_{2,\text{phase/mag}}$ is much larger. The time traces are taken for several field orientations φ and display a strong modulation which is evidenced by taking the fast Fourier transform of each trace. This phenomenon originates from ESEEM where the Hahn-echo decay is modulated by the coupling between the erbium ion and its neighboring tungsten atoms of ^{183}W (*46*). As shown on Fig. S7B and Fig. S8B, the modulation frequencies are angular dependent due to the anisotropy of the dipolar coupling between erbium and tungsten.

Moreover, the data presented in Fig. S7 and Fig. S8 are taken with two resonators which have slightly different frequencies and more importantly different resonance linewidths. The resonance linewidth κ combined with the excitation pulse bandwidth $\Delta\omega_{\text{pulse}}$ filters out high frequencies of the theoretical ESEEM. In Fig. S7, $\kappa/2\pi = 270\,\text{kHz}$ and $\Delta\omega_{\text{pulse}}/2\pi \approx 250\,\text{kHz}$ so modulation frequencies larger than $125\,\text{kHz}$ are filtered out. In Fig. S8, $\kappa/2\pi = 580\,\text{kHz}$ and $\Delta\omega_{\text{pulse}}/2\pi \approx 1\,\text{MHz}$ so modulation frequencies larger than $290\,\text{kHz}$ are filtered out.
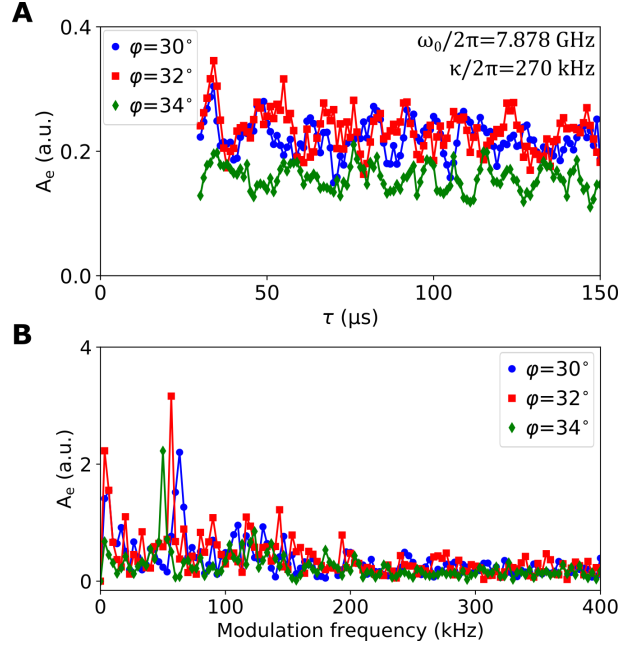
Figure S7: **Electron spin echo envelope modulation measured with resonator 3.** (**A**) Echo amplitude averaged in quadrature as a function of short inter-pulse delay τ, measured at $10\,\mathrm{mK}$ and with different field orientations φ. The resonance has a frequency $\omega_0/2\pi = 7.878\,\mathrm{GHz}$ and a linewidth $\kappa/2\pi = 270\,\mathrm{kHz}$. $4\,\mu s$-long square pulses are used such that the pulse bandwidth is $\Delta\omega_{\mathrm{pulse}}/2\pi \approx 250\,\mathrm{kHz}$. (**B**) Fast Fourier transform of the data of subplot (A).

1.8 $\mathbf{T_2}$ measurements and instantaneous diffusion

Spin coherence is determined by several electric and magnetic interactions which contribute to the decay of the echo amplitude according to

$$A_e(2\tau) = e^{-\sum_i \left(\frac{2\tau}{T_{2,i}}\right)^{x_i}} \tag{10}$$

where $T_{2,i}$ is the coherence time and x_i the exponent due to interaction mechanism i.

In this work, we consider three dominant magnetic interactions: spectral diffusion (SD) due to the nuclear spin bath, SD due to other paramagnetic impurities and instantaneous diffusion (ID). SD has already been mentioned in the main text and comes from the magnetic interaction of the erbium ions with all other electron and nuclear spins in the bath. ID is also a common decoherence mechanism and comes from the magnetic interaction between all erbium spins
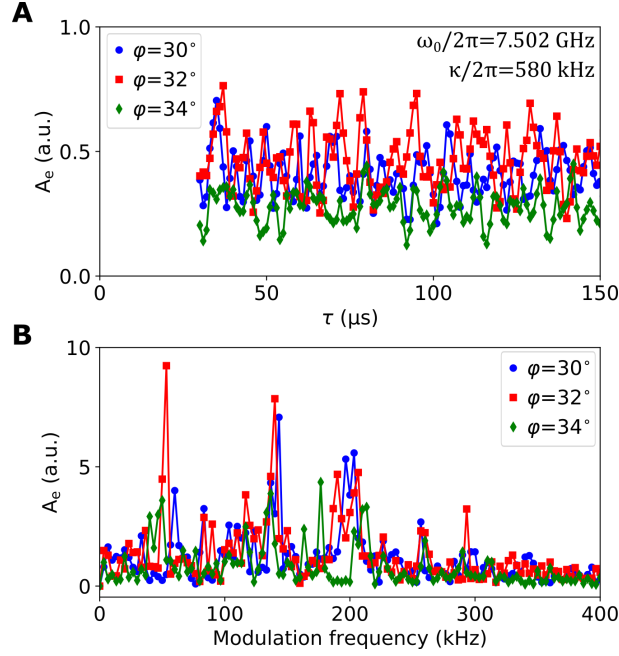
Figure S8: **Electron spin echo envelope modulation measured with resonator 2.** (**A**) Echo amplitude averaged in quadrature as a function of short inter-pulse delay τ, measured at $10\,\mathrm{mK}$ and with different field orientations φ. The resonance has a frequency $\omega_0/2\pi = 7.502\,\mathrm{GHz}$ and a linewidth $\kappa/2\pi = 580\,\mathrm{kHz}$. $1\,\mu s$-long square pulses are used such that the pulse bandwidth is $\Delta\omega_{\mathrm{pulse}}/2\pi \approx 1\,\mathrm{MHz}$. (**B**) Fast Fourier transform of the data of subplot (A).

which are resonant with the microwave excitation pulses.

In this section we estimate at $\varphi = 47°$ the decoherence due to ID and compare it with the measured coherence time presented in Fig. 2.

ID is expected to give an exponential decay $A_{e,\mathrm{ID}}(2\tau) = e^{-2\tau/T_{2,\mathrm{ID}}}$ (*6, 47*) with

$$\frac{1}{T_{2,\mathrm{ID}}} = \frac{5}{2}\frac{\mu_0}{4\pi}\frac{(g\mu_B)^2}{\hbar}\rho\frac{\Delta\omega}{\Gamma}\sin^2\frac{\theta_2}{2},\tag{11}$$

where μ_B is the Bohr magneton, $\rho = 0.77[\mathrm{Er}^{3+}]$ is the zero nuclear-spin isotopes erbium concentration, $\Delta\omega$ is the excitation bandwidth, Γ the spin inhomogeneous linewidth, and θ_2 the refocusing angle.

For the measurement of Fig. 2, $4\,\mu s$-long pulses were used, giving a excitation pulse bandwidth of $\Delta\omega_{\mathrm{pulse}}/2\pi \approx 250\,\mathrm{kHz}$. This is slightly smaller than the resonance linewidth

$\kappa/2\pi = 350\,\text{kHz}$, which is thereby barely filtering the input pulses and $\Delta\omega \approx \Delta\omega_{\text{pulse}}$.

ID is caused by the fraction of excited erbium ions which has an effective concentration $\tilde{\rho} = \rho\Delta\omega/\Gamma$. As Γ is of the order of $10\,\text{MHz}$, $\tilde{\rho} \sim 1.7 \times 10^{11}\,\text{cm}^{-3}$ and the distance between two excited erbium ions is typically $2\,\mu\text{m}$. Here, excited spins are in the bulk (few tens of μm away from the surface) and those within a few μm distance from each other experience approximately the same Rabi angles. Because spins contributing mostly to the Hahn-echo undergo rotations of first $\theta_1 \sim \pi/2$ then $\theta_2 \sim \pi$, their excited neighbours also rotate with similar angles and $\sin(\theta_2/2)^2$ can be approximated to 1.

For $\varphi = 47°$, the inhomogeneous linewidth $\Gamma/2\pi$ was measured to be $10\,\text{MHz}$ (Fig. 1E) and equation 11 gives $T_{2,\text{ID}} \sim 400$ ms. This value is more than one order of magnitude larger than the measured coherence time of Fig. 2 and indicates that ID is not the dominant source of decoherence at this angle.

However, the contribution of ID increases when the spin linewidth Γ gets narrower or when the excitation bandwidth $\Delta\omega$ increases. To evidence the presence of ID, the coherence time measurement of Fig. 2 can be repeated at $\varphi \sim 31°$, where the spin linewidth is the narrowest, and also with a different resonator with a broader resonance linewidth.

Fig. S9 shows this measurement for a resonance linewidth of $\kappa/2\pi = 580\,\text{kHz}$ with two field orientations $\varphi = 47°$ and $\varphi = 32°$. Here, $1\,\mu\text{s}$-long pulses where used, giving an pulse bandwidth of $\Delta\omega_{\text{pulse}} \approx 1\,\text{MHz}$. The resonance linewidth is $\kappa/2\pi = 580\,\text{kHz}$ hence the excitation bandwidth is limited by κ: $\Delta\omega \approx \kappa$.

At $\varphi = 47°$, $\Gamma = 11\,\text{MHz}$ and equation 11 yields $T_{2,\text{ID}} \sim 190$ ms. At $\varphi = 32°$, $\Gamma = 1.8\,\text{MHz}$ and equation 11 yields $T_{2,\text{ID}} \sim 31$ ms.

The resonance linewidth of this measurement is broader than the one used to measure the data of Fig. 2 and the pulses are shorter. As a consequence, high frequencies of ESEEM are less filtered and ESEEM is stronger. Therefore the data are taken in packets of points spaced
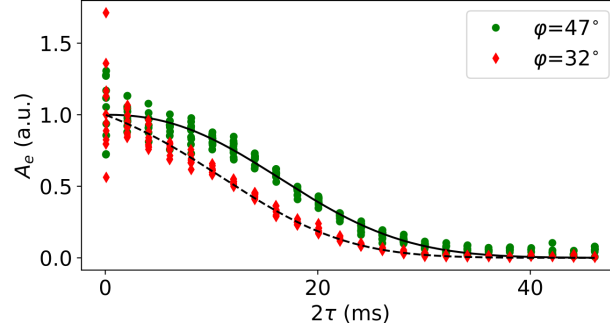
Figure S9: **Electron spin coherence measurements at 10 mK for two magnetic field orientations.** The measurements are performed at $\varphi = 47°$ (circles) and $\varphi = 32°$ (diamonds), with a resonance at $\omega_0/2\pi = 7.502\,\mathrm{GHz}$ and with linewidth $\kappa/2\pi = 580\,\mathrm{kHz}$. Each packet of points is sampled with $\Delta\tau = 2\,\mu\mathrm{s}$ in order to account for ESEEM. The data are averaged in magnitude. The solid black line is a fit with $A_e^2 = e^{-2[(2\tau/T_{2,n})^{x_n} + (2\tau/T_{2,p})^{x_p}]} + C$ where $T_{2,n} = 27.2\,\mathrm{ms}$ and $x_n = 2.74$ are taken from the CCE simulation. The fit yields $T_{2,p} = 28\pm1\,\mathrm{ms}$ and $x_p = 2.1\pm0.2$. The dashed black line is a fit which includes ID, $A_e^2 = e^{-2[(2\tau/T_{2,n})^{x_n} + (2\tau/T_{2,p})^{x_p} + 2\tau/T_{2,\mathrm{ID}}]} + C$. At $\varphi = 32°$, the CCE simulation predicts $T_{2,n} = 24.7\,\mathrm{ms}$ and $x_n = 2.74$. $T_{2,p}$ and x_p are fixed from the fitted values at $\varphi = 47°$. Fitting the remaining ID contribution yields $T_{2,\mathrm{ID}} = 33 \pm 2\,\mathrm{ms}$. The offset C has been subtracted from data and fits (square roots of negative noise on A_e^2 are obviously absent from the plot).

by $\Delta\tau = 2\,\mu\mathrm{s}$ in order to sample the ESEEM properly. The data is fitted in magnitude with the three mentioned decoherence mechanisms,

$$A_e^2(2\tau) = e^{-2[(\frac{2\tau}{T_{2,n}})^{x_n} + (\frac{2\tau}{T_{2,p}})^{x_p} + \frac{2\tau}{T_{2,\mathrm{ID}}}]} + C, \tag{12}$$

where $T_{2,n}$ and x_n correspond to spectral diffusion due to the nuclear spin bath, $T_{2,p}$ and x_p to spectral diffusion due to other paramagnetic impurities and $T_{2,\mathrm{ID}}$ to instantaneous diffusion.

At $\varphi = 47°$, ID is negligible as calculated above. The CCE simulation gives $T_{2,n} = 27.2\,\mathrm{ms}$ and $x_n = 2.74$. Fitting the paramagnetic contribution yields $T_{2,p} = 28\pm1\,\mathrm{ms}$ and $x_p = 2.1\pm0.2$. This value is smaller than what is shown in Fig. 2B where $T_{2,p} \sim 40\,\mathrm{ms}$ at $10\,\mathrm{mK}$ and could be due to the fact that these data were taken in different runs. The data of Fig. S9 yields a total coherence time of $T_2 = 20.5 \pm 0.2\,\mathrm{ms}$ instead of $23.2 \pm 0.5\,\mathrm{ms}$.

At $\varphi = 32°$, the CCE simulation gives $T_{2,n} = 24.7\,\mathrm{ms}$ and $x_n = 2.74$. The paramagnetic

contribution can be taken as independent of angle φ because these impurities have a dilute concentration and are mostly in tetragonal sites with their g-factor being independent of φ. Hence we keep the values extracted at $\varphi = 47°$, namely $T_{2,p} = 28\,\mathrm{ms}$ and $x_p = 2.1$. Fitting only the remaining contribution from ID yields $T_{2,\mathrm{ID}} = 33 \pm 2\,\mathrm{ms}$ which is close to the estimation above and confirms that ID is not negligible at angles where the erbium inhomogeneous linewidth is the narrowest.

1.9 Longitudinal relaxation (T$_1$) measurements

We measure the relaxation time T_1 as a function of cryostat temperature, with sufficient power to address spins in the bulk of the material (Fig. S10). We observe that the temperature dependence is well-fitted by the direct-phonon process (*38*)

$$T_1 = T_{1,0\mathrm{K}} \tanh \frac{\hbar\omega_0}{2k_0 T}, \tag{13}$$

where $T_{1,0\mathrm{K}}$ is the extrapolated relaxation time at zero temperature, confirming that multiphonon processes are not relevant at sub-Kelvin temperatures.
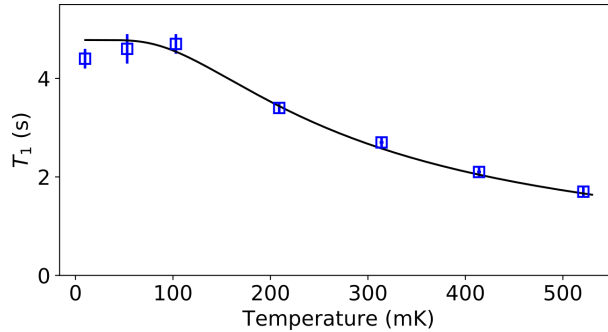

Figure S10: **Longitudinal relaxation time as a function of temperature.** Relaxation time at high input pulse power as a function of cryostat temperature (squares). The solid line is a fit with $T_1 = T_{1,0\mathrm{K}} \tanh (\hbar\omega_0/2k_B T)$ as is predicted for the spin-lattice relaxation time at low temperature. The fit yields $T_{1,0\mathrm{K}} = 4.8 \pm 0.1\,\mathrm{s}$.

## 1.10 Simulations of spin-relaxation power dependence

The numerical simulations presented in Fig. 3B take into account a distribution of Larmor frequencies δ with respect to the resonator frequency and a distribution of spin-resonator coupling constants g_0, the two distributions being independent (*24*).

- for the $2\ \mu m$ wide inductance wire, there are 420 discrete frequency bins taken with uniform spacing between -4κ and 4κ, where $\kappa/2\pi = 185\,\mathrm{kHz}$, and 120 values of coupling strength $g_0/2\pi$, equally spaced between 1 and $1000\,\mathrm{Hz}$,

- for the $5\ \mu m$ wide inductance wire, there are 480 discrete frequency bins taken with uniform spacing between -3.5κ and 3.5κ, where $\kappa/2\pi = 350\,\mathrm{kHz}$, and 120 values of coupling strength $g_0/2\pi$, equally spaced between 0.5 and $500\,\mathrm{Hz}$.

Each spin with frequency detuning δ and coupling constant g_0 relaxes with rate $\Gamma = \Gamma_P + \Gamma_{sl}$, where Γ_{sl} is the spin-lattice relaxation rate and $\Gamma_P = \frac{\kappa g_0^2}{\kappa^2/4 + \delta^2}$ is the Purcell relaxation rate (*37*). For spins at a distance greater than approximately $15\ \mu$m from the inductance wire, the relaxation is dominated by Γ_{sl}, whereas for spins located closer to the indutance wire, it is dominated by Γ_P.

The inhomogeneous absorption linewidth at $\varphi = 30°$ is $\Gamma/2\pi = 2\,\mathrm{MHz}$, which is nearly one order of magnitude wider than the broadest resonance linewidth. Thus the spin frequency distribution ρ_δ is taken as constant. The coupling constant distribution ρ_{g_0} behaves approximately as $1/g_0^3$ at low g_0 and shows a peak at high g_0 due to the spins located close to the wire. The exact profile is calculated using a COMSOL simulation of the magnetic field $\mathbf{B_1}$ generated around the inductance wire with a $1\,\mathrm{A}$ current. The simulation result must then be rescaled by $\delta I = \omega_0 \sqrt{\frac{\hbar}{2Z_0}}$, the rms vacuum fluctuation of the current in the resonator. The resonator impedance $Z_0 \sim 40\ \Omega$ is simulated using the software Ansys HFSS. The computation of the

coupling g_0 is shown in Fig. 1C at $\varphi = 51°$ (i.e. when the magnetic field $\mathbf{B_0}$ is applied parallel to the wire) and the g_0 histogram at $\varphi = 30°$ used for the simulations is shown in Fig. S11.
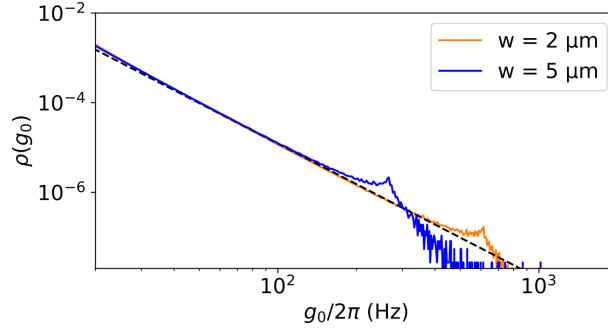
Figure S11: **Spin-resonator coupling distribution**. The coupling distribution is shown in logarithmic scale for the 2 μm and 5 μm wide inductor resonators simulated at $\varphi = 30°$. The COMSOL simulation takes into account spins located in a surface $L_y \times L_z = 400 \times 200$ μm^2 below the inductance wire. Dashed black line is a fit with $\rho(g_0) \propto g_0^{-3}$. The peak at high coupling corresponds to spins located close to the wire.

For simplicity, the simulated pulse sequence for obtaining T_1 is the inversion recovery sequence ($\beta - T - \beta/2 - \tau - \beta - \tau -$ echo), even when CPMG sequences have been used to measure it.

2 Theoretical part

2.1 Model

The spin Hamiltonian can be written

$$H = H_{\mathrm{Er}} + H_{\mathrm{n}} + H_{\mathrm{int}}. \tag{14}$$

The first term,

$$H_{\mathrm{Er}} = \mu_B \mathbf{B}_0 \cdot \mathbf{g} \cdot \mathbf{S}, \tag{15}$$

is the Zeeman energy of the effective spin-1/2 $\mathbf{S}$ of the zero-nuclear-spin isotopes of Er^{3+} under a magnetic field $\mathbf{B}_0$, where μ_B is the Bohr magneton and the g-factor tensor $\mathbf{g}$ has a diagonal form in the crystal frame with $\mathrm{g}_\perp = \mathrm{g}_{aa} = \mathrm{g}_{bb}$ and $\mathrm{g}_\parallel = \mathrm{g}_{cc}$.

The second term,

$$H_{\mathrm{n}} = \mathrm{g}_{\mathrm{n}}\mu_{\mathrm{n}} \sum_i \mathbf{B}_0 \cdot \mathbf{I}_i + \sum_{i<j} \mathbf{I}_i \cdot \mathbb{D}_{ij} \cdot \mathbf{I}_j, \tag{16}$$

is the energy of the bath of ^{183}W nuclear spins ($I_i = 1/2$), where g_{n} is the g-factor of ^{183}W nuclear spins, μ_{n} is the nuclear magneton, μ is the vaccum permeability, and $\mathbb{D}_{ij} = \mu/(4\pi)\mathrm{g}_{\mathrm{n}}^2\mu_{\mathrm{n}}^2 \left(r_{ij}^{-3} - 3\mathbf{r}_{ij}\mathbf{r}_{ij}/r_{ij}^5 \right)$ with $\mathbf{r}_{ij} = \mathbf{r}_j - \mathbf{r}_i$ the displacement between the i-th and j-th nuclear spins.

The third term,

$$H_{\mathrm{int}} = \sum_i \mathbf{S} \cdot \mathbb{A}_i \cdot \mathbf{I}_i, \tag{17}$$

is the dipolar hyperfine interaction, where $\mathbb{A}_i = \mu/(4\pi)\mu_B\mathrm{g}_{\mathrm{n}}\mu_{\mathrm{n}} \left[\mathbf{g}/r_i^3 - 3\left(\mathbf{g}\cdot\mathbf{r}_i\right)\mathbf{r}_i/r_i^5\right]$.

We set the z-axis along $\mathbf{B}_0$ (in the ab-plane with an angle φ from the a-axis). Since the electron Zeeman energy is much stronger than the hyperfine interaction and the nuclear Zeeman energy is much stronger than the nuclear dipolar interaction, we make the secular approximation, dropping the terms that do not conserve the Zeeman energies, such as the $S_{x/y}$ terms, the $I_{x/y}$ terms, which induce electron spin echo enveloppe modulation (ESEEM), and the $I_i^{x/y}I_j^z$ terms.

Therefore, the Hamiltonian becomes a pure dephasing model

$$H \approx |1\rangle\langle 1| \otimes H^{(+)} + |0\rangle\langle 0| \otimes H^{(-)}, \tag{18}$$

with the central-spin-conditional bath Hamiltonian

$$H^{(\pm)} = \pm\frac{\omega}{2} \pm \frac{1}{2}\sum_i \hat{\mathbf{z}} \cdot \mathbb{A}_i \cdot \hat{\mathbf{z}} I_i^z + H_\mathrm{n}. \tag{19}$$

The Hahn echo signal is

$$A_e \propto \mathcal{L}\left(2\tau\right) =$$
$$\mathrm{Tr}\left(\rho_\mathrm{n} e^{iH^{(-)}\tau} e^{iH^{(+)}\tau} e^{-iH^{(-)}\tau} e^{-iH^{(+)}\tau}\right), \tag{20}$$

where ρ_n is the initial bath density matrix (which we choose as the infinite high-temperature thermalized state since the nuclear Zeeman energy is much less than 10 mK).

2.2 Cluster correlation expansion

The central spin coherence is calculated using the cluster correlation expansion (CCE) (*32*), in which the decoherence caused by a cluster of M bath spins $(1, 2, \ldots, M)$ is denoted as $\mathcal{L}_{1,2,\ldots,M}$. The irreducible correlation of a cluster is defined recursively as $\tilde{\mathcal{L}}_j = \mathcal{L}_j$, $\tilde{\mathcal{L}}_{i,j} \equiv \mathcal{L}_{i,j}\tilde{\mathcal{L}}_i^{-1}\tilde{\mathcal{L}}_j^{-1}$, etc., that is, the decoherence function divided by all irreducible correlations of all sub-clusters. For the M-order truncation (CCE-M), the calculation takes into account the irreducible correlations up to the clusters of M spins, $\mathcal{L} \approx \mathcal{L}^{(M)}$, with

$$\mathcal{L}^{(M)} =$$
$$\prod_{i_1} \tilde{\mathcal{L}}_{i_1} \prod_{j_1<j_2} \tilde{\mathcal{L}}_{j_1,j_2} \cdots \prod_{k_1<k_2\cdots<k_M} \tilde{\mathcal{L}}_{k_1,k_2,\ldots,k_M}. \tag{21}$$

With the secular approximation, the CCE-1 contribution (decoherence due to single-spin dynamics, which also causes the ESEEM for relatively strongly coupled nuclear spins) vanishes.

In the simulation, we place the ^{183}W nuclear spins (with a natural abundance $p_\mathrm{n} = 0.145$) randomly on the CaWO$_4$ lattice sites of tungsten ions and the Er^{3+} ions randomly substituting

Ca^{2+}. The bath includes all nuclear spins within a sphere of radius of 11 nm around the central spin. We numerically checked that a larger bath size produces nearly the same result. The numerical simulation also show that the simulation using one specific spatial configuration of [183]W nuclear spins in the lattice is nearly the same as ensemble average over many (50) different spatial configurations. We have checked the convergence of the CCE and found that CCE-3 and CCE-2 produce nearly identical results.

2.3 Simulation results

Fig. S12 compares the CCE-2 simulation in a lattice spin bath according to $CaWO_4$ crystal structure and in an amorphous bath, where the [183]W have same concentration but are placed randomly in space, in order to compare with (*17*). In the amorphous case, the decoherence is significantly faster than in a lattice bath. Such difference can be understood from the fact that the lattice structure sets a lower bound on the distance between nuclear spins, which has a sizeable effect when the spin concentration is not too small.
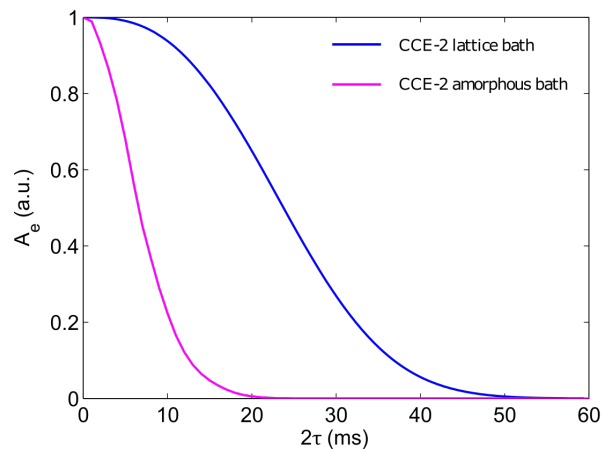

Figure S12: **CCE-2 simulation of the spin decoherence.** The results are fitted by $A_e = e^{-(2\tau/T_2)^x}$, with $T_2 = 27$ ms and $x = 2.7$ for the decoherence in a lattice spin bath (blue line) and $T_2 = 8.05$ ms and $x = 1.88$ for the decoherence in an amorphous bath (pink line). The parameters of the simulations are the magnetic field $B_0 = 67$ mT, the field orientation $\varphi = 46.5°$ and the temperature $T = 10$ mK.

REFERENCES AND NOTES

1. E. Saglamyurek, J. Jin, V. B. Verma, M. D. Shaw, F. Marsili, S. W. Nam, D. Oblak, W. Tittel, Quantum storage of entangled telecom-wavelength photons in an erbium-doped optical fibre. *Nat. Photonics* **9**, 83–87 (2015).

2. M. Afzelius, N. Sangouard, G. Johansson, M. U. Staudt, C. M. Wilson, Proposal for a coherent quantum memory for propagating microwave photons. *New J. Phys.* **15**, 065008 (2013).

3. S. Probst, H. Rotzinger, A. V. Ustinov, P. A. Bushev, Microwave multimode memory with an erbium spin ensemble. *Phys. Rev. B* **92**, 014421 (2015).

4. L. A. Williamson, Y.-H. Chen, J. J. Longdell, Magneto-optic modulator with unit quantum efficiency. *Phys. Rev. Lett.* **113**, 203601 (2014).

5. X. Fernandez-Gonzalvo, Y.-H. Chen, C. Yin, S. Rogge, J. J. Longdell, Coherent frequency up-conversion of microwaves to the optical telecommunications band in an Er:YSO crystal. *Phys. Rev. A* **92**, 062313 (2015).

6. A. M. Tyryshkin, S. Tojo, J. J. L. Morton, H. Riemann, N. V. Abrosimov, P. Becker, H.-J. Pohl, T. Schenkel, M. L. W. Thewalt, K. M. Itoh, S. A. Lyon, Electron spin coherence exceeding seconds in high-purity silicon. *Nat. Mater.* **11**, 143–147 (2012).

7. T. Böttger, C. Thiel, R. Cone, Y. Sun, Effects of magnetic field orientation on optical decoherence in $Er^{3+}:Y_2SiO_5$. *Phys. Rev. B* **79**, 115104 (2009).

8. B. Merkel, A. Ulanowski, A. Reiserer, Coherent and Purcell-enhanced emission from erbium dopants in a cryogenic high-Q resonator. *Phys. Rev. X* **10**, 041025 (2020).

9. M. Zhong, M. P. Hedges, R. L. Ahlefeldt, J. G. Bartholomew, S. E. Beavan, S. M. Wittig, J. J. Longdell, M. J. Sellars, Optically addressable nuclear spins in a solid with a six-hour coherence time. *Nature* **517**, 177–180 (2015).

10. A. Ortu, A. Tiranov, S. Welinski, F. Frowis, N. Gisin, A. Ferrier, P. Goldner, M. Afzelius, Simultaneous coherence enhancement of optical and microwave transitions in solid-state electronic spins. *Nat. Mater.* **17**, 671–675 (2018).

11. J. V. Rakonjac, Y.-H. Chen, S. P. Horvath, J. J. Longdell, Long spin coherence times in the ground state and in an optically excited state of $^{167}Er^{3+}$:Y_2SiO_5 at zero magnetic field. *Phys. Rev. B* **101**, 184430 (2020).

12. G. Wolfowicz, A. M. Tyryshkin, R. E. George, H. Riemann, N. V. Abrosimov, P. Becker, H.-J. Pohl, M. L. W. Thewalt, S. A. Lyon, J. J. L. Morton, Atomic clock transitions in silicon-based spin qubits. *Nat. Nanotechnol.* **8**, 561–564 (2013).

13. V. Ranjan, J. O'Sullivan, E. Albertinale, B. Albanese, T. Chanelière, T. Schenkel, D. Vion, D. Esteve, E. Flurin, J. Morton, P. Bertet, Multimode storage of quantum microwave fields in electron spins over 100 ms. *Phys. Rev. Lett.* **125**, 210505 (2020).

14. M. H. Abobeih, J. Cramer, M. A. Bakker, N. Kalb, M. Markham, D. J. Twitchen, T. H. Taminiau, One-second coherence for a single electron spin coupled to a multi-qubit nuclear-spin environment. *Nat. Commun.* **9**, 2552 (2018).

15. S. Chen, M. Raha, C. M. Phenicie, S. Ourari, J. D. Thompson, Parallel single-shot measurement and coherent control of solid-state spins below the diffraction limit. *Science* **370**, 592–595 (2020).

16. B. Merkel, P. C. Fariña, A. Reiserer, Dynamical decoupling of spin ensembles with strong anisotropic interactions. *Phys. Rev. Lett.* **127**, 030501 (2021).

17. S. Kanai, F. J. Heremans, H. Seo, G. Wolfowicz, C. P. Anderson, S. E. Sullivan, G. Galli, D. D. Awschalom, H. Ohno, Generalized scaling of spin qubit coherence in over 12,000 host materials. arXiv:2102.02986 (2021).

18. W. B. Mims, K. Nassau, J. D. McGee, Spectral diffusion in electron resonance lines. *Phys. Rev.* **123**, 2059–2069 (1961).

19. A. Antipin, A. Katyshev, I. Kurkin, L. Shekun, Paramagnetic resonance and spin-lattice relaxation of Er^{3+} and Tb^{3+} ions in $CaWO_4$ crystal lattice. *Sov. Phys. Solid State* **10**, 468 (1968).

20. P. Haikka, Y. Kubo, A. Bienfait, P. Bertet, K. Moelmer, Proposal for detecting a single electron spin in a microwave resonator. *Phys. Rev. A* **95**, 022306 (2017).

21. A. Erb, J.-C. Lanfranchi, Growth of high-purity scintillating CaWO4 single crystals for the low-temperature direct dark matter search experiments CRESST-II and EURECA. *CrystEngComm* **15**, 2301–2304 (2013).

22. A. Bienfait, J. J. Pla, Y. Kubo, M. Stern, X. Zhou, C. C. Lo, C. D. Weis, T. Schenkel, M. L. W. Thewalt, D. Vion, D. Esteve, B. Julsgaard, K. Mølmer, J. J. L. Morton, P. Bertet, Reaching the quantum limit of sensitivity in electron spin resonance. *Nat. Nanotechnol.* **11**, 253–257 (2016).

23. V. Ranjan, S. Probst, B. Albanese, T. Schenkel, D. Vion, D. Esteve, J. J. L. Morton, P. Bertet, Electron spin resonance spectroscopy with femtoliter detection volume. *Appl. Phys. Lett.* **116**, 184002 (2020).

24. V. Ranjan, S. Probst, B. Albanese, A. Doll, O. Jacquot, E. Flurin, R. Heeres, D. Vion, D. Esteve, J. J. L. Morton, P. Bertet, Pulsed electron spin resonance spectroscopy in the Purcell regime. *J. Magn. Reson.* **310**, 106662 (2020).

25. C. Macklin, K. O'Brien, D. Hover, M. E. Schwartz, V. Bolkhovsky, X. Zhang, W. D. Oliver, I. Siddiqi, A near-quantum-limited Josephson traveling-wave parametric amplifier. *Science* **350**, 307–310 (2015).

26. W. B. Mims, R. Gillen, Broadening of paramagnetic-resonance lines by internal electric fields. *Phys. Rev.* **148**, 438–443 (1966).

27. W. B. Mims, Electric field shift in paramagnetic resonance for four ions in a calcium tungstate lattice. *Phys. Rev.* **140**, A531–A535 (1965).

28. T. Böttger, C. W. Thiel, Y. Sun, R. L. Cone, Optical decoherence and spectral diffusion at 1.5 μm in $Er^{3+}:Y_2SiO_5$ versus magnetic field, temperature, and Er^{3+} concentration. *Phys. Rev. B* **73**, 075101 (2006).

29. S. Bertaina, S. Gambarelli, A. Tkachuk, I. N. Kurkin, B. Malkin, A. Stepanov, B. Barbara, Rare-earth solid-state qubits. *Nat. Nanotechnol.* **2**, 39–42 (2007).

30. P.-Y. Li, C. Liu, Z.-Q. Zhou, X. Liu, T. Tu, T.-S. Yang, Z.-F. Li, Y. Ma, J. Hu, P.-J. Liang, X. Li, J.-Y. Huang, T.-X. Zhu, C.-F. Li, G.-C. Guo, Hyperfine structure and coherent dynamics of rare-earth spins explored with electron-nuclear double resonance at subkelvin temperatures. *Phys. Rev. Appl.* **13**, 024080 (2020).

31. W. M. Witzel, R. de Sousa, S. Das Sarma, Quantum theory of spectral-diffusion-induced electron spin decoherence. *Phys. Rev. B* **72**, 161306 (2005).

32. W. Yang, R.-B. Liu, Quantum many-body theory of qubit decoherence in a finite-size spin bath. *Phys. Rev. B* **78**, 085315 (2008).

33. A. M. Tyryshkin, S. A. Lyon, A. V. Astashkin, A. M. Raitsimring, Electron spin relaxation times of phosphorus donors in silicon. *Phys. Rev. B* **68**, 193207 (2003).

34. N. Sangouard, C. Simon, H. de Riedmatten, N. Gisin, Quantum repeaters based on atomic ensembles and linear optics. *Rev. Mod. Phys.* **83**, 33–80 (2011).

35. S. Takahashi, R. Hanson, J. van Tol, M. S. Sherwin, D. D. Awschalom, Quenching spin decoherence in diamond through spin bath polarization. *Phys. Rev. Lett.* **101**, 047601 (2008).

36. M. Rančić, M. P. Hedges, R. L. Ahlefeldt, M. J. Sellars, Coherence time of over a second in a telecom-compatible quantum memory storage material. *Nat. Phys.* **14**, 50–54 (2018).

37. A. Bienfait, J. Pla, Y. Kubo, X. Zhou, M. Stern, C.-C. Lo, C. Weis, T. Schenkel, D. Vion, D. Esteve, J. Morton, P. Bertet, Controlling spin relaxation with a cavity. *Nature* **531**, 74–77 (2016).

38. A. Abragam, B. Bleaney, *Electron Paramagnetic Resonance of Transition Ions* (OUP Oxford, 2012); Google-Books-ID: ASNoAgAAQBAJ.

39. A. A. Antipin, L. A. Bumagina, B. Z. Malkin, R. M. Rakhmatullin, Anisotropy of Er^{3+} spin-lattice relaxation in $LiYF_4$ crystals. *Soviet J. Exp. Theor. Phys.* **23**, 2700–2707 (1981).

40. B. Albanese, S. Probst, V. Ranjan, C. W. Zollitsch, M. Pechal, A. Wallraff, J. J. L. Morton, D. Vion, D. Esteve, E. Flurin, P. Bertet, Radiative cooling of a spin ensemble. *Nat. Phys.* **16**, 751–755 (2020).

41. R. M. Golding, M. Kestigian, C. W. Tennant, EPR of high-spin Fe^{3+} in calcium tungstate, $CaWO_4$. *J. Phys. C Solid State Phys.* **11**, 5041–5049 (1978).

42. I. Diniz, S. Portolan, R. Ferreira, J. M. Gérard, P. Bertet, A. Auffèves, Strongly coupling a cavity to inhomogeneous ensembles of emitters: Potential for long-lived solid-state quantum memories. *Phys. Rev. A* **84**, 063810 (2011).

43. V. Ranjan, G. de Lange, R. Schutjens, T. Debelhoir, J. P. Groen, D. Szombati, D. J. Thoen, T. M. Klapwijk, R. Hanson, L. DiCarlo, Probing dynamics of an electron-spin ensemble via a superconducting resonator. *Phys. Rev. Lett.* **110**, 067004 (2013).

44. Y. Kubo, F. R. Ong, P. Bertet, D. Vion, V. Jacques, D. Zheng, A. Dréau, J.-F. Roch, A. Auffeves, F. Jelezko, J. Wrachtrup, M. F. Barthe, P. Bergonzo, D. Esteve, Strong coupling of a spin ensemble to a superconducting resonator. *Phys. Rev. Lett.* **105**, 140502 (2010).

45. W.-L. Ma, G. Wolfowicz, N. Zhao, S.-S. Li, J. J. L. Morton, R.-B. Liu, Uncovering many-body correlations in nanoscale nuclear spin baths by central spin decoherence. *Nat. Commun.* **5**, 4822 (2014).

46. S. Probst, G. Zhang, M. Rančić, V. Ranjan, M. Le Dantec, Z. Zhang, B. Albanese, A. Doll, R. B. Liu, J. Morton, T. Chanelière, P. Goldner, D. Vion, D. Esteve, P. Bertet, Hyperfine spectroscopy in a quantum-limited spectrometer. *Magn. Reson.* **1**, 315–330 (2020).

47. A. Schweiger, G. Jeschke, *Principles of Pulse Electron Paramagnetic Resonance* (Oxford Univ. Press, 2001).